=== **NONLINEAR ACOUSTICS** ===

Wide-Angle Parabolic Approximation for Modeling High-Intensity Fields from Strongly Focused Ultrasound Transducers

P. V. Yuldashev[a], *, I. S. Mezdrokhin[a], and V. A. Khokhlova[a]

[a]*Moscow State University, Physics Faculty, Moscow, 119991 Russia*

*e-mail: petr@acs366.phys.msu.ru

Abstract—A novel numerical algorithm based on the wide-angle parabolic approximation is developed for modeling linear and nonlinear fields generated by axially symmetric ultrasound transducers. An example of a strongly focused single-element transducer is used to compare the results of ultrasound field simulations based on the Westervelt equation, Khokhlov–Zabolotskaya–Kuznetsov (KZK) equation with differently modified boundary condition, and nonlinear wide-angle parabolic equation. It is demonstrated that having a computational speed comparable to modeling the KZK equation, the use of wide-angle parabolic approximation makes it possible to obtain solutions for highly focused ultrasound beams that are closer in accuracy to solutions based on the Westervelt equation.

INTRODUCTION

During the last decade, high-intensity focused ultrasound (HIFU) has been emerging to a broader range of noninvasive surgery applications for thermal and mechanical tissue ablation in various organs [1, 2]. The distinctive features of HIFU transducers are large focusing angles and strong degree of nonlinear acoustic effects, particularly in novel applications based on the use of shock-wave exposures [2, 3]. To ensure the efficiency and safety of ultrasound surgical devices in clinical use, it is necessary to quantitatively characterize the parameters of ultrasound fields generated by HIFU transducers in water and in biological tissue; such characterization can aid the assessment of risks and efficacy of a treatment.

When novel medical devices are being developed, calibration characteristics of ultrasound fields they generate are first determined when focusing in water [4]. For this purpose, numerical simulations based on experimental data obtained for a specific transducer can serve as a powerful performance-testing tool. Recently, such measurement-based simulation method for ultrasound field characterization was proposed and receives acceptance in various laboratories around the world [5–7]. The method is based on measurements of the linear pressure field to set exact boundary condition to a wave model. Then, a series of numerical simulations of nonlinear pressure field is conducted over the range of transducer operating power outputs. Simulation accuracy is controlled by comparing the modeling results with measurements of acoustic pressure waveforms at the focus. An important particular geometry of ultrasound fields generated by ultrasound surgery transducers are fields possessing an axial symmetry. First, most applications use transducers in the shape of a single spherical segment [5, 7] or in the form of an annular array [8]. In addition, even the fields of more complex transducers, including multi-element arrays, can be approximated with high accuracy by the field of an equivalent single-element circular transducer [9]. Therefore, an important theoretical and practical problem for ultrasound medical applications is the development of efficient and accurate methods for numerical simulations of nonlinear axially symmetric focused beams.

Current wave models used in medical acoustics are different in the accuracy of describing nonlinear and diffraction effects, the limits of applicability, and the complexity of numerical calculations. One of the most complete wave models is the Westervelt equation, which exactly takes into account the diffraction effects [6, 9, 10]. However, for an axially symmetric field, this equation has the drawback of requiring unreasonably high computational costs. A widely used approximate model for describing axially symmetric beams is the non-linear Khokhlov–Zabolotskaya–Kuznetsov (KZK) equation, which accounts for diffraction effects in the parabolic approximation and therefore is valid only for small focusing angles [11]. The capabilities of using the parabolic model for HIFU transducers has been

successfully extended by modifying the boundary condition to the model. This approach named as an equivalent source method has been shown to yield accurate results in the focal region of the beam [9, 12]. The Padé approximation method is less frequently used but potentially more exact model for describing diffraction effects in the focused axially symmetric fields of medical transducers [13−17]. Such method is often called as a wide-angle approximation, which can also be considered as a generalization of the parabolic model.

The wide-angle approximation has been successfully used in describing the propagation of low-frequency linear sound waves in models of marine media [15, 16]. It has been also applied for nonlinear problems of simulating weakly nonlinear fields in water [17] and air [18]. Various methods have been used to approximate an exact propagator of the one-way wave equation. For example, in [17], the propagator was approximated by the Nth-order rational function, and in [18], by the sum of first-order rational functions. As a result, when calculating the diffraction operator, according to [18], the transverse Laplacian appears only in the left-hand side of the corresponding equation, and in [17], symmetrically on the left- and right-hand sides. This makes the numerical algorithm of [18] close to totally implicit scheme, with all its shortcomings, while the algorithm of [17] is close to the Crank−Nicolson scheme. To calculate the nonlinear operator, a spectral approach has been used in [17, 18], which limited the implementation of the method to solving only weakly linear problems.

This study is based on using the wide-angle approximation in constructing a novel numerical algorithm for simulating both linear and strongly nonlinear ultrasound fields generated by axially symmetric focused transducers used in ultrasound surgery. The novelty of the algorithm is the implementation of a shock-capturing numerical scheme to calculate the nonlinear operator and thus the possibility of modeling ultrasound fields with shock fronts [10]; the method for approximating the exact propagator corresponds to [17]. Another important difference of the present work is the formulation of the boundary condition to the wave model. In [17], it was set in a plane as a circular source with uniformly distributed pressure and phase variation that provided focusing. In our study, a realistic boundary condition was obtained by calculating the Rayleigh integral over the surface of an arbitrary shape radiating onto the initial plane. This approach makes it possible to simulate fields of realistic medical ultrasound transduces having, e.g., a shape of a spherical segment.

To test the accuracy of the new algorithm, field-simulation results obtained using the Westervelt equation [9, 10], the KZK equation [9], and the developed wide-angle parabolic equation were compared. It is demonstrated that the use of wide-angle approxima-

tion makes it possible to simulate the fields of strongly focused axially symmetric sources over the entire spatial domain of the beam with an accuracy close to that provided by the Westervelt equation. However, the computational complexity of the algorithm is comparable to the standard algorithms for solving the KZK equation.

THEORETICAL METHOD

A. The Westervelt and KZK Equations

The Westervelt equation that governs the propagation of nonlinear acoustic waves in arbitrary directions has the form

$$\Delta p' - \frac{1}{c_0^2}\frac{\partial^2 p'}{\partial t^2} = -\frac{\varepsilon}{\rho_0 c_0^4}\frac{\partial^2}{\partial t^2}\left(p'^2\right) - \frac{\delta}{2c_0^3}\frac{\partial^3 p'}{\partial t^3}. \tag{1}$$

Here $p'(t, x, y, z)$ is the acoustic pressure, t is the time, Δ is the Laplace operator $\Delta = \partial^2/\partial x^2 + \partial^2/\partial y^2 + \partial^2/\partial z^2$ in the Cartesian coordinate system (x, y, z); ρ_0, c_0, ε, and δ are the density, sound velocity, nonlinearity coefficient, and thermoviscous absorption coefficient of the propagation medium, respectively. The physical parameters in Eq. (1), that correspond to propagation in water at a temperature of $20°C$, are $\rho_0 = 998$ kg/m³, $c_0 = 1486$ m/s, $\varepsilon = 3.5$, and $\delta = 4.33 \times 10^{-6}$ m²/s [6, 9].

To model an ultrasound beam generated by an axially symmetric source in a homogeneous medium, i.e., in the absence of reflections and backscattering effects, the Eq. 1 can be rewritten in the retarded coordinate system:

$$\frac{\partial^2 p}{\partial \tau \partial z} = \frac{\partial^2 p}{\partial z^2} + \frac{1}{r}\frac{\partial}{\partial r}\left(r\frac{\partial p}{\partial r}\right) + \frac{\varepsilon}{2\rho_0 c_0^3}\frac{\partial^2 p^2}{\partial \tau^2} + \frac{\delta}{2c_0^3}\frac{\partial^3 p}{\partial \tau^3}, \tag{2}$$

where $p(\tau, r, z) = p'(t, x, y, z)$, $\tau = t - z/c_0$, $r = \sqrt{x^2 + y^2}$ is the radial coordinate in the plane perpendicular to the axis of symmetry of the source. In the parabolic approximation, the Eq. 2 is reduced to the KZK equation:

$$\frac{\partial^2 p}{\partial \tau \partial z} = \frac{1}{r}\frac{\partial}{\partial r}\left(r\frac{\partial p}{\partial r}\right) + \frac{\varepsilon}{2\rho_0 c_0^3}\frac{\partial^2 p^2}{\partial \tau^2} + \frac{\delta}{2c_0^3}\frac{\partial^3 p}{\partial \tau^3}. \tag{3}$$

Both Eqs. (2) and (3) are evolutionary in terms of the coordinate z, i.e. the pressure $p(\tau, r, z)$ slowly changes as a function of z, and rapid phase changes are taken into account by introducing the delayed time τ in the accompanying coordinate system. The KZK equation (3) differs from the Westervelt equation (2) only by the absence of the second order partial derivative of pressure over the coordinate z in the right-hand side of the equation. This difference is related to the

use of a simplifying assumption on the smallness of the diffraction angles in the KZK equation, whereas the diffraction part of the Westervelt Eqs. (1) and (2) exactly corresponds to the linear wave equation. Assuming nonlinear and thermoviscous absorption coefficients equal to zero in Eqs. (2) and (3), the corresponding linear wave equations describing only the diffraction effects are obtained.

B. Wide-Angle Parabolic Approximation

The wide-angle parabolic approximation can be considered, on the one hand, as a generalization of the standard parabolic diffraction operator in the Eq. (3), and, on the other hand, as one of the ways to construct an approximate solution to the diffraction part of the Eqs. (1) and (2). Consider the derivation of the wide-angle approximation equation for individual harmonic components in the Fourier series expansion $p'_\omega(\omega, r, z) = \int p' \exp(-i\omega t) dt$ of the pressure field $p'(t, r, z)$ in Eq. (1). In the absence of nonlinear effects and absorption, the Eq. (1) yields the Helmholtz equation for the complex amplitude p'_ω:

$$\Delta p'_\omega + k^2 p'_\omega = 0, \qquad (4)$$

where $k = \omega/c_0$ is the wavenumber. If we introduce the differential operators $\hat{L}$ and $\hat{Q}$ as

$$\hat{L} = \frac{1}{k^2} \frac{1}{r} \frac{\partial}{\partial r}\left(r \frac{\partial}{\partial r}\right), \quad \hat{Q}^2 = 1 + \hat{L}, \qquad (5)$$

then the Helmholtz equation can be represented as

$$\frac{\partial^2 p'_\omega}{\partial z^2} + k^2 \hat{Q}^2 p'_\omega = 0. \qquad (6)$$

Taking into account that for a homogeneous medium considered here the wavenumber k does not depend on the spatial coordinates, the Helmholtz equation splits into two independent equations:

$$\frac{\partial p'_\omega}{\partial z} + ik\hat{Q}p'_\omega = 0, \qquad (7a)$$

$$\frac{\partial p'_\omega}{\partial z} - ik\hat{Q}p'_\omega = 0, \qquad (7b)$$

each of which corresponds to waves traveling at acute angles in either the negative (7a) or the positive (7b) directions of the axis z [13].

The operator $\hat{Q} = \sqrt{1 + \hat{L}}$ is a psuedodifferential operator, which can be represented as the Fourier transform $\overline{p}'_\omega(\omega, k_\perp, z)$ of the complex pressure amplitude $p'_\omega(\omega, r, z)$ over the transverse spatial coordinates

multiplied by the corresponding transfer function. The representation

$$\hat{Q}p'_\omega = \sqrt{1 + \hat{L}} p'_\omega, \qquad (8)$$

therefore means that for the Fourier transforms of the left- and right-hand sides of the Eq. (8), the following equation is valid:

$$\mathrm{F}\left\{\hat{Q}p'_\omega\right\} = \sqrt{1 - \frac{k_\perp^2}{k^2}} \overline{p}'_\omega, \quad k_\perp < k. \qquad (9)$$

Here the operator $\mathrm{F}\{\cdot\}$ means finding Fourier transform of the function that is the argument of the operator over the transverse spatial coordinates. The contribution of the components of the spatial Fourier spectrum of the field for $k_\perp > k$ can be neglected, since they correspond to rapidly attenuating evanescent waves.

To obtain the wide-angle approximation, consider the accompanying coordinate system, in which the slowly varying complex amplitude p is used instead of the pressure amplitude $p'_\omega(\omega, r, z)$:

$$p'_\omega(r, z) = p_\omega(r, z) e^{ikz}. \qquad (10)$$

In this case, the Eq. (7b) for one-way propagation along the positive direction of the axis z transforms to

$$\frac{\partial p_\omega}{\partial z} - ik\left(\sqrt{1 + \hat{L}} - 1\right)p_\omega = 0. \qquad (11)$$

The operator $\hat{Q} = \sqrt{1 + \hat{L}}$ can be represented as a Taylor series in terms of powers of the operator $\hat{L}$:

$$\hat{Q} = 1 + \sum_{n=1}^{\infty} q_n \hat{L}^n. \qquad (12)$$

Retaining in the Eq. (11) a finite number of terms in series of the Eq. (12), different approximate solutions can be obtained. If the expansion is limited to the linear term, then $\hat{Q} = 1 + \hat{L}/2$, and the Eq. (11) transforms to the standard parabolic diffraction equation for the frequency components $p_\omega = \int p \exp(-i\omega\tau) d\tau$ in the lossless linearized KZK equation (3):

$$\frac{\partial p_\omega}{\partial z} = \frac{i}{2k} \frac{1}{r} \frac{\partial}{\partial r}\left(r \frac{\partial p_\omega}{\partial r}\right). \qquad (13)$$

Retaining higher-order terms in the expansion (12), more accurate wide-angle parabolic approximation equations can be obtained. For the purpose of constructing numerical schemes and their solutions, there is no advantage in using such expansions because such equation includes higher-order spatial derivatives that correspond to integer powers of the operator $\hat{L}$. Therefore, in practice, the approximate equation is constructed differently [15].

If the distribution of the pressure amplitude p_ω is known at a distance z along the transverse coordinate r, then the solution to the Eq. (11) at the step $z + \Delta z$ can be represented as [13]

$$p_\omega(r, z + \Delta z) = \exp\left[ik\Delta z\left(\sqrt{1 + \hat{L}} - 1\right)\right] p_\omega(r, z), \quad (14)$$

where the operator

$$\hat{A} = \exp\left[ik\Delta z\left(\sqrt{1 + \hat{L}} - 1\right)\right] \quad (15)$$

is termed as the propagator. The propagator $\hat{A}$, similar to the operator $\hat{Q}$, can be approximated by the first several terms in the Taylor series for the operator $\hat{L}$. However, as mentioned above, such representation is not practical. Therefore, the propagator is more often represented as a rational function: the ratio of two polynomials of the degree N, which is also called the Padé or the split-step Padé approximation [13]:

$$\hat{A}_P = \frac{a_0 + a_1\hat{L} + \cdots + a_N\hat{L}^N}{b_0 + b_1\hat{L} + \cdots + b_N\hat{L}^N}. \quad (16)$$

The coefficients of the Padé approximation can be found if the coefficients for expansion of the propagator into a Taylor series are known up to the $2N$ inclusively. The coefficients a_0 and b_0 in the Eq. (16) are equal to unity. The larger is the number N, the better approximation of the initial propagator (15) is achieved by the Eq. (16). In this study, the value of $N = 4$ was used. Then, each of the polynomials was factored resulting in the following representation of the propagator (16):

$$\hat{A}_P = \frac{a_0 \prod\limits_{n=1}^{N}\left(1 + \mu_n\hat{L}\right)}{b_0 \prod\limits_{n=1}^{N}\left(1 + \nu_n\hat{L}\right)}, \quad (17)$$

where $\mu_n = -1/\alpha_n$, $\nu_n = -1/\beta_n$, and α_n and β_n are the roots of the corresponding polynomials in the numerator and denominator of the Padé approximation. To calculate the roots, an algorithm based on the Aberth–Erlich method was used [19]. The representation (17) for the propagator admits an iterative solution procedure at each step Δz in the form

$$\left(1 + \nu_n\hat{L}\right) p_\omega^{(n+1)}(z + \Delta z, r)$$
$$= \left(1 + \mu_n\hat{L}\right) p_\omega^{(n)}(z, r), \quad n = 1 \ldots N. \quad (18)$$

The iterative procedure (18) was realized here in four steps, sequentially for each of the $N = 4$ pairs of values for coefficients ν_n and μ_n. The phase error (in radians) between the exact propagator, Eq. (15), and its approximate representation, Eq. (18), for the first harmonic was 2.7×10^{-5} over one step Δz and 0.15 in total over the entire calculation domain for waves

propagating at an angle of 65° to the source axis. Each of the Eqs. (18) contains only the first power of the second-order differential operator $\hat{L}$, which makes it possible to use simple finite-difference schemes to construct a numerical solution. The wide-angle parabolic equation thus can be represented as the Padé approximation (16) of the exact propagator (15) of the one-way wave equation (11).

C. Boundary Conditions in the Source Plane

To solve the evolutionary equations (2, 3, 11, a boundary condition should be set as a pressure field distribution in some initial plane perpendicular to the source axis. As an example, consider the field generated by a single-element strongly focused source in the form of a spherical segment with the radius of $a = 5$ cm, focal distance of $F = 9$ cm, and operating frequency of $f = 1$ MHz (Fig. 1) [9, 20]. The half-angle of focusing for such a source is $\theta = 33.7°$, and the coefficient of linear pressure amplification at the focus in comparison to the pressure at the source surface is 64 [9]. If the source surface oscillates in a piston mode with vibrational velocity amplitude u_0, then the characteristic pressure amplitude at the source surface can be determined in the plane wave approximation as $p_0 = \rho_0 c_0 u_0$.

The boundary condition for the standard parabolic equation (3) is usually set in the plane $z = 0$ as the pressure amplitude distribution at the source operating frequency and is described by the expression

$$p_{\omega_0}(r, z = 0) = p_0 \exp\left(-ik_0 r^2/2F\right), \quad r \le a,$$
$$p_{\omega_0}(r, z = 0) = 0, \quad r > a. \quad (19)$$

Here, $\omega_0 = 2\pi f$ is the circular frequency, $k_0 = \omega_0/c_0$ is the wavenumber, a is the radius of the source in the plane that coincides with radius of the real source (solid lines in Figs. 1a, 1b). However, it is well known that with an increase in the convergence angle of the source, the solution to the standard parabolic model starts to deviate from the exact solution to the diffraction problem in the form of the Rayleigh integral [21]. To extend the applicability limits of the parabolic approximation, it has been proposed to use a modified boundary condition in the form of an equivalent source [9, 12]. The parameters of the equivalent source in the boundary condition (19) were chosen by matching the pressure amplitudes at the focus and the positions of the first diffraction zeros of the main focal maximum at the beam axis for solutions obtained with the parabolic model and with the Rayleigh integral. Analytic expressions were obtained for the radius a_M, focal distance F_M, and initial pressure amplitude p_M of the equivalent source as functions of a, F, and p_0 of the spherically focused source
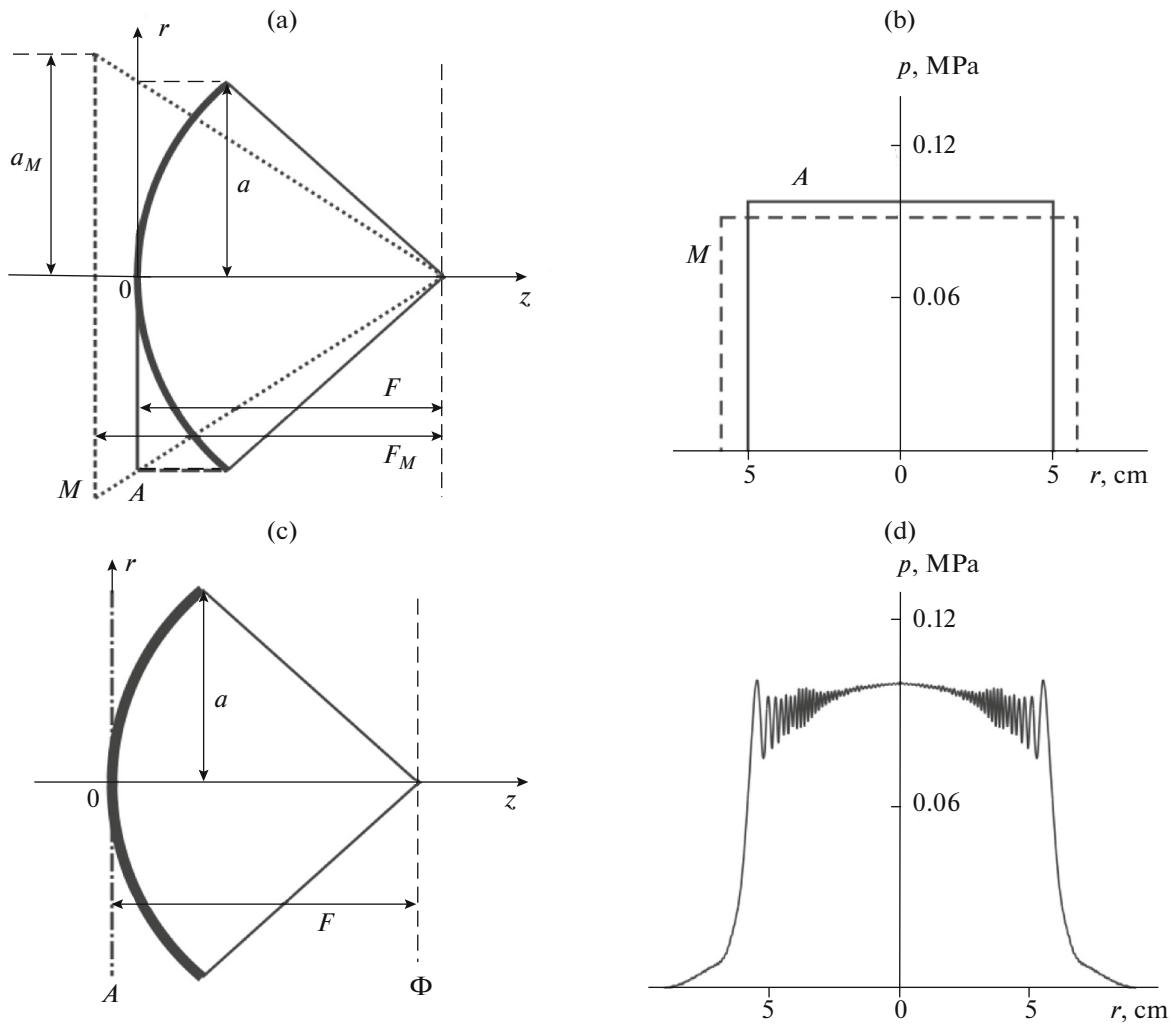
Fig. 1. Illustration of methods for setting a boundary condition in various models of ultrasound beam generated by a single-element focused transducer of 1 MHz operating frequency, 5 cm radius of aperture, and 9 cm focal length. For parabolic equation (a, b): uniform distribution of the pressure amplitude is given in the plane A passing through the transducer center while for an equivalent source the boundary condition is set in the plane M. For wide-angle parabolic equation (c, d): the field is transferred first from the transducer surface to the plane Φ using the Rayleigh integral, then to the plane A using the angular spectrum method.

for different values of the dimensionless parameter $k_0 a$. It was also demonstrated that the values of F_M and a_M (dashed lines in Fig. 1a, 1b) always exceeded the corresponding values of F and a, and the difference between them increased with an increase in the convergence angle of the source. Below, both the standard formulation (19) and the equivalent source model are used for setting a boundary condition to the KZK equation.

For the Westervelt equation (2) and the wide-angle parabolic model (11), the boundary condition was set in two steps. First, the Rayleigh integral [20]

$$p'(\mathbf{r}) = -i\rho_0 c_0 \frac{k}{2\pi} \int_S \frac{u(\mathbf{r}')e^{ik|\mathbf{r}-\mathbf{r}'|}}{|\mathbf{r}-\mathbf{r}'|} dS \qquad (20)$$

was used to calculate the acoustic pressure distribution in the focal plane (see Fig. 1c). Here, $p'(\mathbf{r})$ in the complex pressure amplitude at the observation point with the radius vector $\mathbf{r}$ and $\mathbf{r}'$ is the radius vector of an element at the source surface dS. The value of the normal component of the oscillation velocity $u(\mathbf{r}')$ at the surface of the source was assumed to be uniform. Integration in the Eq. (20) was performed along the surface S, which is the segment of a sphere bounded by a polar angle θ (Fig. 1). Then, the obtained pressure amplitude distribution was transferred to the plane $z = 0$ using the angular spectrum method [10]. As shown in Fig. 1d, the resultant pressure amplitude distribution at $z = 0$ has a nonuniform structure along the ra-

dial coordinate and is notable different from the rectangular distributions of the parabolic models in Fig. 1b.

D. Boundary Conditions over the Radial Coordinate

To decrease the effect of the spatial window in simulations along the radial coordinate in the standard and wide-angle parabolic equations, nonreflecting boundary condition of a perfectly matched layer (PML) were used close to the edge of the spatial window of the radial coordinate r [22]. A small near-boundary layer with thickness $W = r_{max} - r_{PML}$ was introduced, in which the radial coordinate r was transformed to the complex value $\tilde{r}$:

$$\tilde{r} = r + \int_{r_{PML}}^{r} \frac{i\sigma(r')}{\omega}dr', \qquad (21)$$

where $\sigma(r)$ is a function of the coordinates that determines attenuation in the PML, r_{PML} is the origin of the PML, and r_{max} is the coordinate for the boundary of the simulation domain chosen equal to $1.4a$. As a result, differential operator $\hat{L}$ within the layer is transformed to

$$\hat{L} = \frac{1}{k^2}\frac{1}{r}\frac{\partial}{\partial r}\left(r\frac{\partial}{\partial r}\right) \rightarrow \frac{1}{k^2}\frac{1}{\tilde{r}}\frac{\partial}{\partial \tilde{r}}\left(\tilde{r}\frac{\partial}{\partial \tilde{r}}\right)$$
$$= \frac{1}{S^2 k^2}\left(\frac{1}{r}\frac{\partial}{\partial r}\left(r\frac{\partial}{\partial r}\right) + \frac{\bar{S}'S - \bar{S}S'}{S\bar{S}}\frac{\partial}{\partial r}\right), \qquad (22)$$

where two functions are introduced,

$$S(r) = 1 + \frac{i\sigma(r)}{\omega} \quad \text{and} \quad \bar{S}(r) = 1 + \frac{1}{r}\int_{r_{PML}}^{r}\frac{i\sigma(r')}{\omega}dr', \quad (23)$$

$S'(r)$ and $\bar{S}'(r)$ denote their derivatives over the coordinate r. These functions differ from unity only within the PML; outside the PML, the differential operator $\hat{L}$ has its initial form (5).

The attenuation function $\sigma(r)$ was chosen following a power law as

$$\sigma(r) = \sigma_0\left(\frac{r - r_{PML}}{r_{max} - r_{PML}}\right)^3. \qquad (24)$$

The value of the coefficient σ_0 and the PML thickness are usually chosen experimentally by minimizing the amplitude of the reflected waves. In this study, σ_0 was chosen exceeding the circular frequency ω_0 by a factor of 10, and the layer width W was chosen equal to 5 mm. The amplitude of the reflected waves was evaluated and shown to be less than -80 dB of the incident wave amplitude.

E. Numerical Algorithms

Numerical solutions to the Eqs. (2) and (3) were calculated following the method of fractional steps with an operator splitting procedure of second-order accuracy over the propagation distance z [23] and a combined time-domain and frequency-domain approach to describe different physical effects at each step of the grid along the beam axis from z to $z + \Delta z$ [6, 10]. The acoustic pressure $p(\tau, r, z)$ at the distance z was represented at each spatial point r either as a temporal pressure waveform or in the form of a finite Fourier series expansion of harmonic components. An adaptive algorithm with varying number of harmonics included in simulations was used at each step over the coordinate z. The number of harmonics increased with increasing distortion of the waveform and corresponding broadening of its spectrum. If the amplitude of the last currently used harmonic exceeded 10^{-6} of the source amplitude, then another $\sqrt{n}$ harmonics were added to the calculation. The maximum number of harmonics was 800.

Since the nonlinear and absorption operators in the Eqs. (2), (3), and (11) are the same, identical methods to calculate them were used. To calculate the nonlinear operator at small distances from the source, a set of coupled equations for the harmonic amplitudes was solved using the fourth-order accuracy Runge−Kutta method. When the amplitude of the tenth harmonic exceeded the amplitude of the fundamental harmonic by 1%, a conservative Godunov-type scheme was applied [10]. The absorption term was calculated using an exact analytic solution for each of the harmonics.

The diffraction operator was calculated in the frequency domain independently for each harmonic component. Due to specific features of the diffraction terms in each model, different numerical methods were applied to calculate them. For the Westervelt equation, analytic solution for the angular spectrum was used; the amplitudes of harmonics were calculated using two-dimensional fast Fourier transform (FFT) in spatial coordinates [10]. Spatial grid steps in the plane xy were $dx = dy = 0.02$ mm, and the step along the axis z, $dz = 0.1$ mm, was the same as the step in the operator splitting procedure.

To calculate the diffraction operator of the standard parabolic approximation, an implicit scheme was used first at distances up to 5% of the focal distance, then, at larger distances, the Crank−Nicolson scheme was applied. The diffraction operator of the wide-angle approximation (18) was calculated using a

scheme similar in structure to the Crank−Nicolson scheme:

$$p_{\omega,j}^{n+1} + \frac{\nu_n}{k^2\Delta r^2}\left(p_{\omega,j+1}^{n+1} - 2p_{\omega,j}^{n+1} + p_{\omega,j-1}^{n+1} \right.$$

$$+ \frac{p_{\omega,j+1}^{n+1} - p_{\omega,j-1}^{n+1}}{2(j-1)} \bigg) = p_{\omega,j}^n + \frac{\mu_n}{k^2\Delta r^2}$$

$$\times \left(p_{\omega,j+1}^n - 2p_{\omega,j}^n + p_{\omega,j-1}^n + \frac{p_{\omega,j+1}^n - p_{\omega,j-1}^n}{2(j-1)} \right), \quad (25)$$

$$n = 1\ldots N, \quad j > 1,$$

$$p_{\omega,j}^{n+1} + \frac{4\nu_n}{k^2\Delta r^2}\left(p_{\omega,j+1}^{n+1} - p_{\omega,j}^{n+1} \right) = p_{\omega,j}^n$$

$$+ \frac{4\mu_n}{k^2\Delta r^2}\left(p_{\omega,j+1}^n - p_{\omega,j}^n \right), \quad n = 1\ldots N, \quad j = 1,$$

where j is the index of the spatial grid node in the radial direction. This system of linear equations for the pressure values at the grid point $p_{\omega,j}^n$ has a tridiagonal matrix and was solved by the standard Thomas algorithm.

Within the PML layer, the finite-difference schemes presented above were modified following the transformation of the operator $\hat{L}$ (22). As a result, the coefficients of the tridiagonal matrix varied. The grid steps of finite-difference schemes were 0.0025 mm along the radial coordinate and 0.025 mm along the z coordinate aligned with the beam axis. For the step over the z coordinate and the wavenumber $k = 4230$ m^{-1} that corresponds to the fundamental frequency, $n = 1$, the values of the coefficients ν_n and μ_n were as follows: $\mu_1 = 0.0295 + 0.0113i$, $\mu_2 = 0.2488 + 0.0089i$, $\mu_3 = 0.5861 + 0.0049i$, $\mu_4 = 0.8828 + 0.0014i$, $\nu_1 = 0.0295 - 0.0113i$, $\nu_2 = 0.2488 - 0.0089i$, $\nu_3 = 0.5861 - 0.0049i$, $\nu_4 = 0.8828 - 0.0014i$.

All of the algorithms were adapted for parallel computing using an OpenMP technology, which resulted in shortening the calculation time in accordance with the number of processor cores involved in calculations (usually from four to eight). Note that in the finite-difference schemes for calculating the diffraction operator of the parabolic equations, it was necessary to use a finer spatial grid (5400 points in the longitudinal direction and 40 000 points in the radial direction) as compared to the Westervelt equation, where an analytic expression for the angular spectrum was used (700 points in the longitudinal direction and 12 800 points in the radial direction). Depending on the degree of nonlinear effects, the algorithm included from 10 to 800 harmonics, and calculation of the three-dimensional Westervelt equation required com-

putational time from several hours to several days; for the KZK and wide-angle parabolic equations, calculations required computational time from tens of minutes to several hours.

RESULTS AND DISCUSSION

A. Comparison of the Results from Linear Beam Simulations

At the first step, the Eqs. (2), (3), and (11) were simulated with nonlinear and absorption operators being switched off. In this way, the differences in the solutions resulting from the differences in diffraction operators of the corresponding wave models were tested. The solution (11) in the form of the Rayleigh integral (20) was considered as a reference.

Figure 2 shows the pressure amplitude distributions along the beam axis z and the transverse coordinate r in the focal plane that were simulated using different models: the Rayleigh integral, the parabolic equation with the standard boundary condition (PE) and the modified boundary condition in the form of an equivalent source (PEE), and the wide-angle parabolic equation (WAPE) with the boundary condition calculated in the initial plane $z = 0$ using the focal plane as an intermediate surface (Fig. 1). Clearly, in the region of several diffraction maxima around the focus, the solutions to the parabolic model with the modified boundary condition and to the wide-angle model are practically indistinguishable from the reference. The solution to the standard parabolic equation notably differs from the reference one both in the pressure amplitude at the focus and in the structure of the diffraction lobes close to the focus, which demonstrates its limited applicability for describing fields generated by highly focused sources.

The differences between the solutions of various models are depicted in more detail in Fig. 3. Two-dimensional distributions are presented in the axial plane zr for the absolute values of the difference between the pressure amplitudes in the reference solution and in the solutions calculated by the above-mentioned methods. The distributions are normalized to the value of the pressure amplitude at the focus in the reference solution. In simulations based on the standard parabolic model, the error in determining the pressure amplitude reaches about 8% at certain individual points not only near the focus, but at some other points close to the beam axis. These differences are mainly related to the inaccuracy of the position of the field maxima and minima with respect to the reference solution. Modification to the boundary condition allows to achieve coincidence of the parabolic and reference solutions within the focal diffraction lobe and good agreement between the solutions over several diffraction lobes around the focus [6, 12]. However, the error in pressure amplitude can reach 6% in the
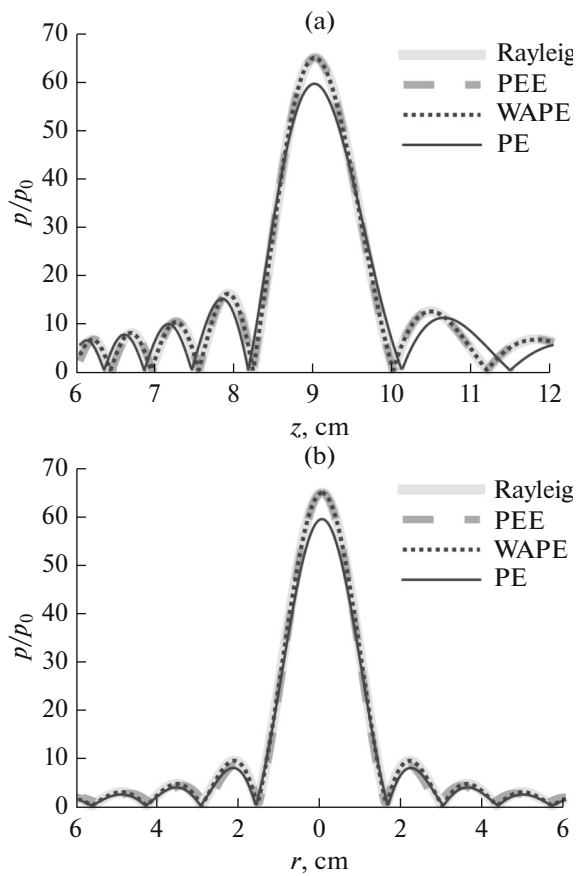
Fig. 2. Pressure amplitude distributions on the transducer axis (a) and in the focal plane (b) normalized by the pressure amplitude on its surface. Notations: Rayleigh, reference solution to diffraction problem in a form of the Rayleigh integral; PEE, solution to the parabolic equation with modified boundary conditions in the form of an equivalent source; WAPE, solution to the wide-angle parabolic equation; PE, solution to the parabolic equation with standard boundary condition.

Fig. 3. Two-dimensional distributions of a difference in pressure amplitudes between the reference and approximate solutions in the axial plane of the beam normalized by the pressure amplitude in the reference solution at the focus. (a) Parabolic equation with standard boundary condition, (b) parabolic equation with modified boundary condition, (c) wide-angle parabolic equation.

near field of the source close the beam axis and at the edges of the beam in the radial direction. These differences are mainly related to the difference in the positions of the maxima and minima of the diffraction field. The most precise agreement with the reference solution is observed for the wide-angle approximation: the error at the focus is less than 0.07%; it is less than 0.5% in the area around the focus; the maximum error does not exceed 2.5% and is observed on the beam axis in the near field of the source. The figure also demonstrates that the pressure amplitude, as well as the positions of the field maxima and minima in the solutions to the wide-angle parabolic equation and the Rayleigh integral correspond well to each other already at distances of $z > 0.5F$.
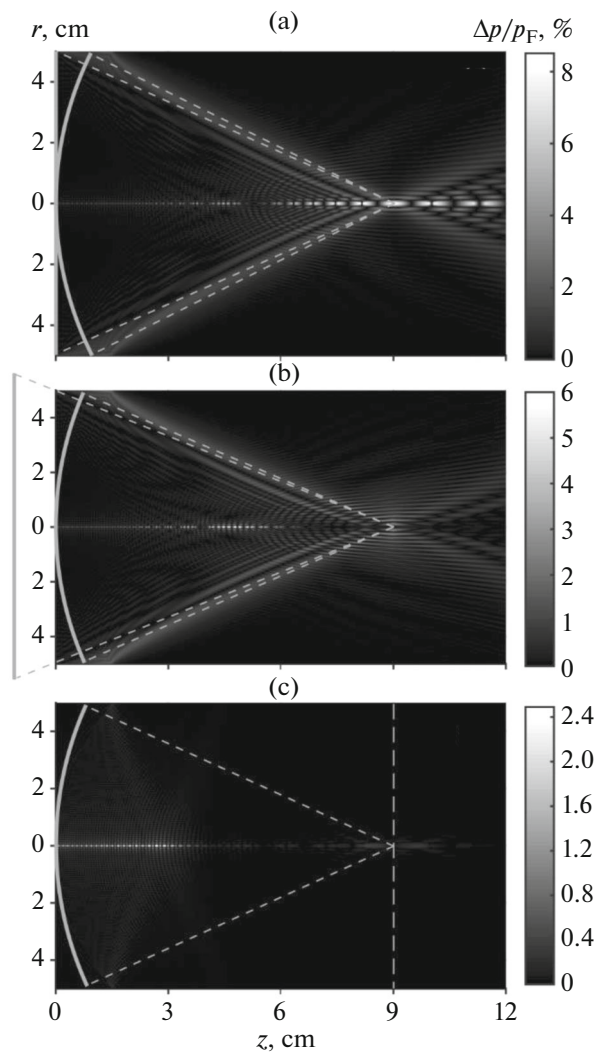
B. Comparison of the Simulation Results for Nonlinear Beams

At the next step, the accuracy of the solutions to the KZK equation with modified boundary condition and to the nonlinear wide-angle parabolic equation was estimated in simulations of nonlinear beams with account for weak thermoviscous absorption. The results were compared to the reference numerical solution to the Westervelt equation. The solution to the KZK equation with standard boundary condition was not considered, since the accuracy of simulating a linear beam already did not seem satisfactory.

Figure 4 shows the distributions of the positive and negative peak pressures in acoustic waveforms along
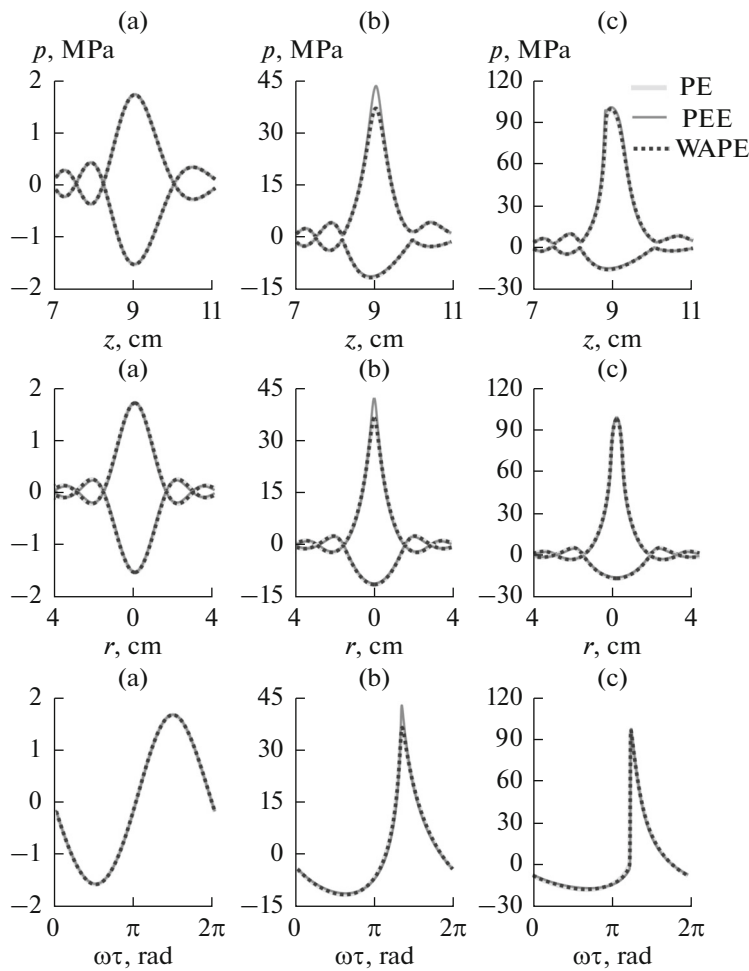
Fig. 4. Distributions of the peak positive and peak negative pressure on the transducer axis (top row), in its focal plane (middle row), and pressure waveforms at the focus (bottom row) for various values of the pressure amplitude at the transducer surface: (a) 0.025, (b) 0.25, (c) 0.45 MPa. Notations: WE, solution to the Westervelt equation; PEE, solution to the parabolic equation with modified boundary condition; WAPE, solution to the wide-angle parabolic equation.

the source axis and in the focal plane, as well as the waveforms at the source focus obtained using the three different wave models for three different pressure amplitudes at the source. For the peak negative pressure, almost no discrepancy can be seen in the results calculated with all three models. For the peak positive pressure, in the case of a quasi-linear beam, $p_0 = 0.025$ MPa (Fig. 4a), when nonlinear waveform distortion and asymmetry in the peak pressure values are small, the results given by all three methods are very close to each other. With an increase in the initial pressure amplitude, starting from $p_0 = 0.15$ MPa, a certain discrepancy occurs in the solution to the parabolic equation with modified boundary condition, which reaches a maximum (18%) at an initial amplitude of $p_0 = 0.25$ MPa (Fig. 4b), when a shock front starts to form at the focus. At the amplitude of $p_0 = 0.45$ MPa (Fig. 4c), a developed shock forms

in the focal waveform; at this level of the waveform distortion, when the ratio of the shock amplitude to the initial pressure at the source reaches its maximum [9], the solutions for the peak positive pressures are again in a good agreement.

Excess values of the peak positive pressure given by the solution to the KZK equation with modified boundary condition in comparison to the reference solution to the Westervelt equation and nonlinear wide-angle parabolic equation can be seen in Fig. 5, where the peak pressures at the geometric focus ($z = F$) are plotted against the pressure amplitude at the source. The growth curve of the peak positive pressure in the solution to the KZK equation clearly goes higher than those in the other solutions. This discrepancy can be explained by certain differences of the numerical algorithms used here. Specifically, the linear beam configurations in different models are estab-
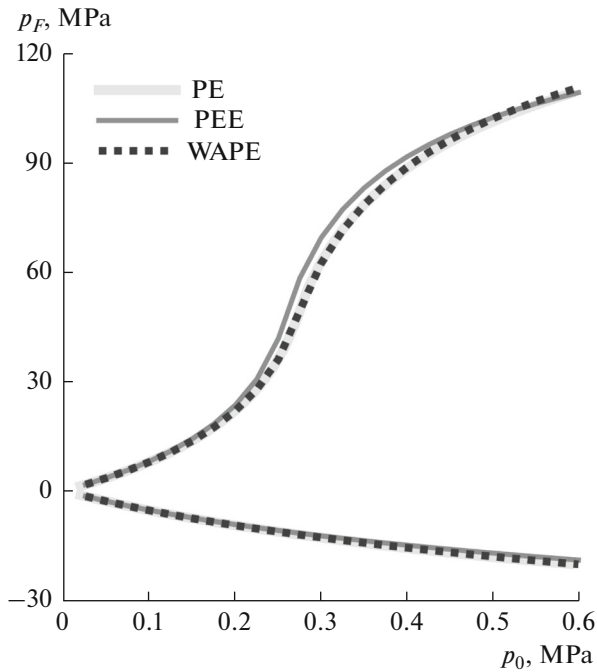
p_F, MPa

Fig. 5. Dependences of the peak positive and peak negative pressure at the focus on the pressure amplitude at the transducer surface. Notation: WE, solution to the Westervelt equation; PEE, solution to the parabolic equation with modified boundary condition; WAPE, solution to the wide-angle parabolic equation.

lished so that they are very close near the focal maximum, whereas some differences are evident outside of the focal lobe (Fig. 3). In the parabolic approximation with modified boundary condition, the focal distance is somewhat larger than for the initial spherically shaped source; i.e., nonlinear effects accumulate over larger distances. In addition, when solving the linear wide-angle and Westervelt equations at small distances, $0 \leq z \leq D$, where $D = F - \sqrt{F^2 - R^2}$ is the depth of the spherical cup, nonlinear effects were included in simulations only within the region bounded by the spherical surface of the source. Thus, it was taken into account that the field behind the source did not contribute to nonlinear propagation effects. In the algorithm simulating the KZK equation, nonlinear effects were included over the entire domain of the propagation distances z. Thus, nonlinear effects were slightly overestimated in the KZK solution when calculating the prefocal region of the beam. Rapid increase of the peak positive pressure with the source amplitude when the shock front begins to form at the focus may be the reason that the sharp increase in the peak positive pressure at the focus in the KZK model occurs at somewhat smaller pressure levels at the source.

CONCLUSIONS

A novel numerical algorithm is presented that allows modeling of nonlinear ultrasound fields generated by axially symmetric focused transducers based on the wide-angle parabolic approximation of the diffraction effects. Validation simulations were conducted for a single-element transducer in the form of a spherical segment with 33.7° half-angle of convergence. It was shown that the wide-angle parabolic approximation makes it possible to calculate both linear and nonlinear fields generated by strongly focused HIFU transducers with a high accuracy, sufficient for practical application.

ACKNOWLEDGMENTS

REFERENCES

1. L. R. Gavrilov, *High Intensity Focused Ultrasound in Medicine* (Fazis, Moscow, 2013) [in Russian].

2. V. A. Khokhlova, J. B. Fowlkes, W. W. Roberts, G. R. Schade, Z. Xu, T. D. Khokhlova, T. L. Hall, A. D. Maxwell, Y. N. Wang, and C. A. Cain, Int. J. Hyperthermia **31** (2), 145 (2015).

3. M. Hoogenboom, D. Eikelenboom, M. H. den Brok, A. Heerschap, J. J. Fütterer, and G. J. Adema, Ultrasound Med. Biol. **41** (6), 1500 (2015).

4. *International Electrotechnical Commission IEC/TS62556. Ultrasonics-Field Characterization − Specification and Measurement of Field Parameters for High Intensity Therapeutic Ultrasound (HITU) Transducers and Systems,* 1.0 ed. (Geneva, 2014).

5. M. S. Canney, M. R. Bailey, L. A. Crum, V. A. Khokhlova, and O. A. Sapozhnikov, J. Acoust. Soc. Am. **124** (4), 2406 (2008).

6. W. Kreider, P. V. Yuldashev, O. A. Sapozhnikov, N. Farr, A. Partanen, M. R. Bailey, and V. A. Khokhlova, IEEE Trans. Ultrason., Ferroelectr. Freq. Control **60** (8), 1683 (2013).

7. O. V. Bessonova and V. Wilkens, IEEE Trans. Ultrason., Ferroelectr. Freq. Control **60** (2), 290 (2013).

8. M. Hoogenboom, M. J. van Amerongen, D. C. Eikelenboom, M. Wassink, and M. H. den Brok, J. Ther. Ultrasound **3**, 3 (2015).

9. P. B. Rosnitskiy, P. V. Yuldashev, O. A. Sapozhnikov, A. Maxwell, W. Kreider, M. R. Bailey, and V. A. Khokhlova, IEEE Trans. Ultrason., Ferroelectr. Freq. Control **64** (2), 374 (2017).

10. P. V. Yuldashev and V. A. Khokhlova, Acoust. Phys. **57** (3), 334 (2011).

11. J. Tjotta, S. Tjotta, and E. Vefring, J. Acoust. Soc. Am. **89** (3), 1017 (1991).

12. P. B. Rosnitskiy, P. V. Yuldashev, B. A. Vysokanov, and V. A. Khokhlova, Acoust. Phys. **62** (2), 151 (2016).

13. M. D. Collins, J. Acoust. Soc. Am. **93** (6), Part 1, 1736 (1993).

14. D. Yevick and D. J. Thomson, J. Acoust. Soc. Am. **108** (6), 2784 (2000).

15. K. V. Avilov, Akust. Zh. **41** (1), 5 (1995).

16. K. V. Avilov, S. N. Kulichkov, and O. E. Popov, in *Proc. 2nd All-Russian Acoustical Conference. Section "Acous-tics of the Ocean"* (Nizhny Novgorod, June 6−9, 2017), pp. 1155−1162.

17. J. E. Soneson, IEEE Trans. Ultrason., Ferroelectr. Freq. Control **64** (4), 679 (2017).

18. T. Kamakura, H. Nomura, and G. T. Clement, Ultrasonics **53**, 432 (2013).

19. D. A. Bini, Numer. Algorithms **13** (2), 179 (1996).

20. K. B. Bader and C. K. Holland, Phys. Med. Biol. **61** (7), 2947 (2016).

21. H. T. O'Neil, J. Acoust. Soc. Am. **21** (5), 516 (1949).

22. J. P. Berenger, J. Comput. Phys. **114**, 185 (1994).

23. R. J. Zemp, J. Tavakkoli, and R. S. Cobbold, J. Acoust. Soc. Am. **113** (1), 139 (2003).